

# An Efficient Second-Order Adaptive Procedure for Inserting CAD Geometries into Hexahedral Meshes using Volume Fractions

Brian N. Granzow<sup>a,\*</sup>, Stephen D. Bond<sup>a</sup>, Michael J. Powell<sup>a</sup>, Daniel A. Ibanez<sup>a</sup>

<sup>a</sup>*Sandia National Laboratories  
P.O. Box 5800  
Albuquerque, NM 87185-1321*

---

## Abstract

This paper is concerned with inserting three-dimensional computer-aided design (CAD) geometries into meshes composed of hexahedral elements using a volume fraction representation. An adaptive procedure for doing so is presented. The procedure consists of two steps. The first step performs spatial acceleration using a  $k$ -d tree. The second step involves subdividing individual hexahedra in an adaptive mesh refinement (AMR)-like fashion and approximating the CAD geometry linearly (as a plane) at the finest subdivision. The procedure requires only two geometric queries from a CAD kernel: determining whether or not a queried spatial coordinate is inside or outside the CAD geometry and determining the closest point on the CAD geometry's surface from a given spatial coordinate. We prove that the procedure is second-order accurate for sufficiently smooth geometries and sufficiently refined background meshes. We demonstrate the expected order of accuracy is achieved with several verification tests and illustrate the procedure's effectiveness for several exemplar CAD geometries.

*Keywords:* CAD geometry, adaptive, volume fractions, hexahedron, unstructured mesh

---

## 1. Introduction

Computational meshes are an inherent component of many numerical methods. Inserting geometric objects into such meshes is often a requisite procedure during simulation initialization, particularly when considering interactions between multiple materials [7, 10, 16, 12, 1]. In this context, the location, orientation, and shape of material interfaces is often encoded in the form of per-material *volume fractions*. A volume fraction denotes the ratio of a material's volume within a given mesh element to the volume of the element itself. This paper is concerned with inserting three-dimensional geometries represented by computer-aided design (CAD) software into meshes composed of *hexahedral* elements via volume fractions.

Prior to our work, a typical state of the art approach for converting a geometry into volume fractions on a mesh (see e.g. [16]) loosely follows these steps:

1. If the geometry is in CAD form, convert it to a triangulated surface via a process known as faceting and store it in a file format such as STL.
2. Implement a method to answer in/out queries (whether a given point is inside or outside the geometry) that may utilize spatial search structures based on the triangulated surface.

---

\*Corresponding author, bngranz@sandia.gov

<sup>1</sup>Sandia National Laboratories is a multimission laboratory managed and operated by National Technology and Engineering Solutions of Sandia LLC, a wholly owned subsidiary of Honeywell International Inc. for the U.S. Department of Energy's National Nuclear Security Administration under contract DE-NA0003525. This article describes objective technical results and analysis. Any subjective views or opinions that might be expressed in the article do not necessarily represent the views of the U.S. Department of Energy or the United States Government.

3. Iterate over every element in the mesh and, within each element, iterate over multiple sample points, performing an in/out query at every sample point.
4. Derive a single volume fraction value for each element based on the in/out results for all the sample points in that element.

Such approaches have a few pain points when performing large-scale simulations:

1. Faceting produces large numbers of triangles for a typical CAD model. The large numbers of triangles cause multiple issues:
  - (a) The resulting STL files consume additional disk space.
  - (b) The full set of triangles may exceed the total memory available to a single processor of a massively parallel computer.
  - (c) Even with spatial acceleration structures, answering in/out queries becomes more and more expensive as the number of triangles grows.
2. The requirement that an in/out query must be performed at every sample point in every element makes the overall approach scale poorly when both the number of triangles and the number of mesh elements grow. Even employing parallelism over the mesh elements at scale does not completely solve this issue.

Our approach differs in a few key ways that address these pain points:

1. Given a point, we are able to directly query the CAD model for whether that point is inside or outside the geometry as well as which point on the CAD surface is closest. This precludes the need to triangulate complex surfaces.
2. By using the concept of a closest point and a bounding sphere, we are able to apply a spatial acceleration tree structure to the mesh elements, producing a method whose runtime scales sublinearly with the number of mesh elements. The performance advantage of our method lies in the number of queries being orders of magnitude smaller than the number of mesh elements.

A key realization is the following: if, given a set of many mesh elements, one can compute a bounding sphere around them and show that the entire bounding sphere is inside or outside the geometry, then all of those mesh elements may be marked as entirely inside or outside the geometry. We then apply this concept hierarchically following the structure of a  $k$ -d tree built from the centroids of the mesh elements to build a hierarchy of bounding spheres of the mesh elements. This spatial acceleration tree structure allows us to avoid querying most of the mesh elements during the volume fraction computation. Within a single element, we adaptively subdivide the element in octree fashion and apply the same bounding sphere concept to guide the subdivision. Finally, for each of the finest subhexahedra, we approximate the CAD geometry’s surface as a plane and compute a volume fraction contribution using the intersection of this plane and the subhex.

The remainder of this paper is structured as follows. First, we provide a detailed description of the proposed volume fraction insertion procedure, as described in three parts: the construction of a  $k$ -d tree based on a given set of hexahedral mesh elements, the use of the  $k$ -d tree to spatially accelerate volume fraction assignment, and the use of an AMR-like procedure to obtain accurate volume fraction representations for individual hexahedra that intersect the CAD geometry’s surface. Next, we prove that this procedure attains second-order accuracy in volume under specific conditions. Lastly, we present results that demonstrate the expected order of accuracy and highlight the effectiveness and efficiency of the procedure.

## 2. Volume Fraction Insertion Procedure

### 2.1. $k$ -d Tree Construction

Let  $\{K^e\}_{e=1}^{n_{el}}$  denote a set of  $n_{el}$  hexahedra with mean coordinate centroids  $\{\mathbf{c}^e\}_{e=1}^{n_{el}}$ . The volume fraction insertion procedure begins by constructing a  $k$ -d tree that spatially partitions the coordinates  $\{\mathbf{c}^e\}_{e=1}^{n_{el}}$  using recursive coordinate bisection [3, 4]. Briefly, the  $k$ -d tree we use is a binary tree that separates coordinates

in  $d$ -dimensional ( $d = 3$  presently) space with axis-aligned hyperplanes. For a given non-leaf node in the tree, recursive coordinate bisection chooses the axis normal to this separating plane as

$$l = \underset{k}{\operatorname{argmax}} \operatorname{diam}(\{e_k \cdot \mathbf{c}^n\}_{n=1}^{n_{\text{node}}}), \quad (1)$$

where  $e_k$  denotes the  $k^{\text{th}}$  basis vector and  $n_{\text{node}}$  denotes the number of centroids associated with the current node. The node’s two children contain  $\lfloor \frac{1}{2}n_{\text{node}} \rfloor$  or  $\lfloor \frac{1}{2}n_{\text{node}} \rfloor + 1$  centroids with  $l$ -coordinate greater than or less than the separating plane’s  $l$ -coordinate, given as:

$$x_l = \frac{1}{n_{\text{node}}} \sum_{n=1}^{n_{\text{node}}} c_l^n. \quad (2)$$

A bounding sphere that fully covers the set of hexahedra associated with a given node is computed and stored for each node in the tree. We conceptually illustrate this  $k$ -d tree in two dimensions in Figure 1. The construction of the  $k$ -d tree occurs once before any geometry is inserted into the mesh and can be reused when inserting multiple geometries.

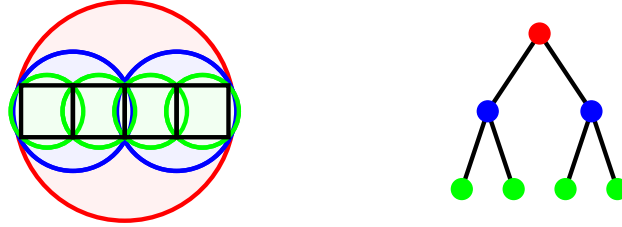


Figure 1: Left: A mesh with four quadrilateral elements (black) and bounding circles associated with nodes in the  $k$ -d tree (red, blue, green). Right: The  $k$ -d tree structure associated with the mesh on the left, where the root node is associated with all mesh elements and leaf nodes are associated with a single mesh element.

## 2.2. Bulk Volume Fraction Sampling

Let  $\Omega \subset \mathbb{R}^3$  denote a bounded domain represented by a CAD kernel with boundary  $\partial\Omega$ . Spatial acceleration for representing the domain  $\Omega$  in the mesh elements  $\{K^e\}_{e=1}^{n_{\text{el}}}$  by volume fractions is achieved by recursively descending the nodes of the  $k$ -d tree. A given node’s bounding sphere is determined to be fully inside, fully outside, or intersecting the geometry  $\Omega$  using two CAD queries, as discussed in the next paragraph. If the bounding sphere is found to be either fully inside or fully outside of  $\Omega$ , then all of the tree node’s hexahedra are assigned volume fractions of one or zero, respectively, and recursion is terminated. If the bounding sphere is found to be intersecting  $\Omega$ , then recursion continues. If the recursion procedure reaches a leaf node, then recursion is terminated and an individual volume fraction is assigned using the AMR-like procedure described in Section 2.3.

To classify a bounding sphere as fully inside, fully outside, or intersecting the geometry  $\Omega$ , the bounding sphere’s center  $\mathbf{x}_c^{\text{sphere}}$  is first determined to be inside or outside of  $\Omega$  using a CAD in/out query. Then the point  $\mathbf{x}_p$  on the geometry’s surface that is closest to the bounding sphere’s center  $\mathbf{x}_c^{\text{sphere}}$  is determined using a CAD closest point query. The Euclidean distance  $d = \|\mathbf{x}_c^{\text{sphere}} - \mathbf{x}_p\|$  from this point to the sphere’s center is computed and compared to the bounding sphere’s radius  $r$ . This leads to four potential scenarios as illustrated by Figure 2. If  $d > r$  and  $\mathbf{x}_c^{\text{sphere}} \notin \Omega$ , then the bounding sphere is fully outside  $\Omega$  (sphere A), if  $d > r$  and  $\mathbf{x}_c^{\text{sphere}} \in \Omega$ , then the bounding sphere is fully inside  $\Omega$  (sphere B), and if  $d < r$ , then the bounding sphere intersects  $\Omega$  (spheres C and D).

**Remark 1.** Floating point precision and other factors in CAD kernel implementations can lead to ‘non-watertight’ geometries, for which in/out CAD queries may not be robust. Strategies exist [8, 15] to generalize the notion of containment within a body that we do not presently consider but could be pursued in future work.

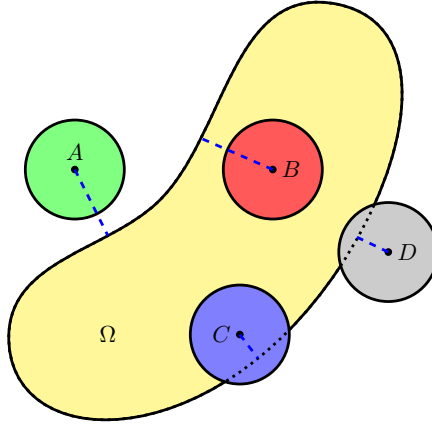


Figure 2: Four potential bounding sphere classifications when comparing the sphere’s radius to the closest distance to the geometry’s surface. (A) The bounding sphere is fully outside of  $\Omega$ . (B) The bounding sphere is fully inside of  $\Omega$ . (C) The bounding sphere intersects  $\Omega$  and its center  $\mathbf{x}_c^C \in \Omega$ . (D) The bounding sphere intersects  $\Omega$  and its center  $\mathbf{x}_c^D \notin \Omega$ .

### 2.3. Adaptive Element Volume Fraction Sampling

Once a leaf in the  $k$ -d tree is reached, the volume of intersection between the leaf’s corresponding mesh hexahedron and the domain  $\Omega$  must be determined. This volume is approximated using an octree, where hexes are recursively subdivided into eight subhexes in an AMR-like fashion. The left image in Figure 3 illustrates this subdivision process in two spatial dimensions. Presently, the number of AMR subdivisions is a user-specified input, where a larger number of subdivisions will correspond to a more accurate volume fraction representation of the domain  $\Omega$ . However, one could envision devising a scheme that locally controls the geometric error to a user-prescribed tolerance. We leave this as an avenue for future research. To determine if an individual subhex is fully inside, fully outside, or intersecting the CAD geometry’s surface, a bounding sphere of the subhex is constructed centered at the subhex’s mean coordinate centroid  $\mathbf{x}_c^{\text{sphere}}$  and the same logic described in the previous section is applied (where a CAD in/out query and a CAD closest point query fully characterizes the subhex’s in/out/intersecting status). Subhexes that are fully outside or fully inside of the domain  $\Omega$  are given subhex volume fractions of zero and one, respectively, and recursion is terminated.

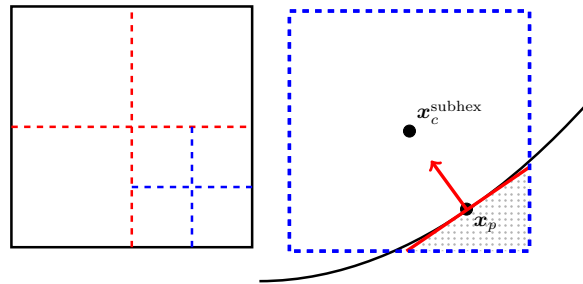


Figure 3: Left: A two-dimensional representation of a hexahedron (solid black) subdivided to two AMR levels. Right: A two-dimensional representation of the intersection of a subhex (dashed blue) with a CAD geometry (solid black line), the planar approximation of the geometry’s surface within the subhex (solid red line), and the plane’s unit normal (solid red line with arrow). The dotted subvolume corresponds to the approximated CAD geometry within the subhex.

At subhexes that have reached the maximal AMR depth, the geometry is approximated by a plane, as illustrated by the right image in Figure 3. The plane is defined by a point  $\mathbf{x}_p$  on the CAD surface and a plane surface normal  $\mathbf{n}_p$ . The point  $\mathbf{x}_p$  is chosen as the the closest point on the geometry’s surface to the the subhex’s mean coordinate centroid  $\mathbf{x}_c^{\text{subhex}}$ . The plane surface normal  $\mathbf{n}_p$  is chosen to be parallel to the vector  $\mathbf{x}_c^{\text{subhex}} - \mathbf{x}_p$ , which is also, by definition, parallel to the geometry’s outward surface normal (as long

as the domain  $K^{\text{subhex}} \cap \Omega$  is simply connected and  $\partial\Omega$  is sufficiently smooth). The normal vector is oriented outward to the surface  $\partial\Omega$  by querying whether the subhex centroid is inside or outside of the domain  $\Omega$ . Using `r3d` [11], the subhex is cut by the constructed plane and the volume  $V^{\text{poly}}$  of the resultant polyhedron is computed. Lastly, the volume fraction  $V^{\text{poly}}/\text{meas}(K^e)$  is contributed to the original hex's total volume fraction. In the degenerate case when the closest point  $\mathbf{x}_p$  is identical to the subhex centroid  $\mathbf{x}_c^{\text{subhex}}$ , we choose a subhex volume fraction of  $\frac{1}{2}$ .

**Remark 2.** If the domain  $K^{\text{subhex}} \cap \Omega$  is not simply connected or contains more than a single surface in the interior of  $K^{\text{subhex}}$  (such as a small filament), then it may be possible to employ more sophisticated techniques [6, 2, 9] to capture and represent the geometry within the mesh. In particular, we propose moment-of-fluid initialization from CAD geometry as an avenue for future research.

### 3. Error Estimate

**Theorem 1.** *For a bounded CAD geometry  $\Omega \subset \mathbb{R}^d$  with a smoothly twice-differentiable boundary,  $\partial\Omega$ , and a sufficiently refined background mesh, the volume insertion error is bounded by  $|V_h - V_{\text{exact}}| \leq Ch^2$ , where  $V_h$  and  $V_{\text{exact}}$  are the approximate and exact volumes, respectively,  $C$  is a constant, and  $h$  is the background element size.*

*Proof.* Let  $f(\mathbf{x}, \Omega)$  denote a signed distance function, defined as

$$f(\mathbf{x}, \Omega) := \begin{cases} -d(\mathbf{x}, \partial\Omega) & \text{if } \mathbf{x} \in \Omega, \\ d(\mathbf{x}, \partial\Omega) & \text{otherwise,} \end{cases}$$

where  $d(\mathbf{x}, \partial\Omega)$  denotes the minimal distance from a point  $\mathbf{x}$  to a surface  $\partial\Omega$ , given as

$$d(\mathbf{x}, \partial\Omega) := \inf_{\mathbf{y} \in \partial\Omega} \|\mathbf{x} - \mathbf{y}\|_2.$$

Note the signed distance  $f$  is positive for points exterior to  $\Omega$  and negative for points interior to  $\Omega$ .

Suppose that the CAD geometry is covered by a mesh  $\mathcal{T} := \cup_e \bar{K}^e$ , with elements  $\{K^e\}_{e=1}^{n_{\text{el}}}$  of size  $h$ . Splitting over elements, the exact volume is

$$V_{\text{exact}} = \sum_{K^e \in \mathcal{T}} \int_{K^e} \Phi(f(\mathbf{x}, \Omega)) \, d\mathbf{x},$$

where  $\Phi$  is the step function

$$\Phi(x) = \begin{cases} 1, & x \leq 0, \\ 0, & \text{otherwise.} \end{cases}$$

Let  $g^e$  be the local linear approximation to  $f$  in element  $K^e$ . Then the approximate volume represented by the volume fraction insertion procedure is

$$V_h = \sum_{K^e \in \mathcal{T}} \int_{K^e} \Phi(g^e(\mathbf{x})) \, d\mathbf{x}.$$

The total volume insertion error can then be bounded above as

$$\begin{aligned} |V_h - V_{\text{exact}}| &= \left| \sum_{K^e \in \mathcal{T}} \left( \int_{K^e} \Phi(f(\mathbf{x}, \Omega)) \, d\mathbf{x} - \int_{K^e} \Phi(g^e(\mathbf{x})) \, d\mathbf{x} \right) \right| \\ &\leq \sum_{K^e \in \mathcal{T}} \int_{K^e} |\Phi(f(\mathbf{x}, \Omega)) - \Phi(g^e(\mathbf{x}))| \, d\mathbf{x}. \end{aligned}$$

For a given  $\mathbf{x}_e \in K^e$ , let  $\mathbf{x}_p \in \partial\Omega$  be the closest point on the CAD geometry surface. Assuming the surface is smoothly differentiable, the first-order constrained optimality condition requires that the gradient of the signed distance function is parallel to the surface normal with

$$\alpha(\mathbf{x}_p - \mathbf{x}_e) = \nabla_{\mathbf{x}} f(\mathbf{x}_p, \Omega) = \mathbf{n}_p,$$

for some scalar  $\alpha$ , where  $\mathbf{n}_p$  is the outward normal to  $\Omega$  at point  $\mathbf{x}_p$ . Using the Taylor series expansion of  $f$  at  $\mathbf{x}_p$ , we find

$$f(\mathbf{x}, \Omega) = f(\mathbf{x}_p, \Omega) + (\mathbf{x} - \mathbf{x}_p) \cdot \nabla_{\mathbf{x}} f(\mathbf{x}_p, \Omega) + \frac{1}{2}(\mathbf{x} - \mathbf{x}_p)^T H_f(\boldsymbol{\xi}, \Omega)(\mathbf{x} - \mathbf{x}_p),$$

where  $H_f$  is the Hessian of the signed distance function and  $\boldsymbol{\xi}$  is some point on the chord connecting  $\mathbf{x}$  and  $\mathbf{x}_p$ . Note that the first two terms of the expansion are exactly the local linear approximation to  $f$  used by the CAD insertion algorithm

$$g^e(\mathbf{x}) = f(\mathbf{x}_p, \Omega) + (\mathbf{x} - \mathbf{x}_p) \cdot \nabla_{\mathbf{x}} f(\mathbf{x}_p, \Omega).$$

In an element of size  $h$ , one can show that

$$|f(\mathbf{x}, \Omega) - g^e(\mathbf{x})| = \left| \frac{1}{2}(\mathbf{x} - \mathbf{x}_p)^T H_f(\boldsymbol{\xi}, \Omega)(\mathbf{x} - \mathbf{x}_p) \right| \leq \tilde{C}h^2, \quad (3)$$

where the constant  $\tilde{C}$  is proportional to the maximum spectral radius of  $H_f$  over the element.

Introduce the functional

$$\Psi(s) := \Phi(sf(\mathbf{x}, \Omega) + (1-s)g^e(\mathbf{x})),$$

and note that  $\Psi(1) = \Phi(f(\mathbf{x}, \Omega))$  and  $\Psi(0) = \Phi(g^e(\mathbf{x}))$ . Applying the mean-value theorem to  $\Psi$ , we obtain

$$\int_{K^e} |\Phi(f(\mathbf{x}, \Omega)) - \Phi(g^e(\mathbf{x}))| d\mathbf{x} = \int_{K^e} |(f(\mathbf{x}, \Omega) - g^e(\mathbf{x}))| \delta(\gamma f(\mathbf{x}, \Omega) + (1-\gamma)g^e(\mathbf{x})) d\mathbf{x},$$

where  $\gamma$  is a scalar on the interval in  $[0, 1]$  and  $\delta$  denotes the Dirac delta function. Using the inequality (3) yields

$$\int_{K^e} |\Phi(f(\mathbf{x}, \Omega)) - \Phi(g^e(\mathbf{x}))| \leq \tilde{C}h^2 \int_{K^e} \delta(\gamma f(\mathbf{x}, \Omega) + (1-\gamma)g^e(\mathbf{x})) d\mathbf{x} \leq \tilde{C}h^2 \hat{C}h^{d-1},$$

where  $\hat{C}h^{d-1}$  is the area of the surface  $\{\mathbf{x} \in K^e \subset \mathbb{R}^d \mid (1-\gamma)f(\mathbf{x}, \Omega) + \gamma g^e(\mathbf{x}) = 0\}$ . Finally, for a regular CAD surface, the number of elements intersecting  $\partial\Omega$  is proportional to  $1/h^{d-1}$ , so that the total volume insertion error is bounded by

$$|V_h - V_{\text{exact}}| \leq \sum_{K^e \in \mathcal{T}} \tilde{C}h^2 \hat{C}h^{d-1} = Ch^2,$$

for some constant  $C$ . □

## 4. Results

In this section, we investigate the efficacy of the proposed volume fraction insertion procedure for a variety of numerical simulations. Throughout, we make reference and comparison to a uniform sampling procedure, which we describe as follows. We consider a reference hexahedron  $K^R := \{\boldsymbol{\xi} : \boldsymbol{\xi} \in [-1, 1]^3\}$  and take the coordinates  $\{\boldsymbol{\xi}_i\}_{i=1}^{n_s}$  defined as the centroids of the subhexes found by uniformly refining the reference hex  $n_{\text{sub}}$  times, so that the total number of sample points is given as  $n_s = (2^{n_{\text{sub}}})^3$ . Each reference coordinate  $\boldsymbol{\xi}_i$  is mapped to a physical coordinate  $\mathbf{x}_i$  using trilinear Lagrange shape functions and a CAD in/out query is performed at this physical coordinate. An element volume fraction is then computed as a Jacobian determinant weighted ratio of the number of sample points found inside the domain  $\Omega$  to the total number of sample points  $n_s$ .

#### 4.1. Verification

In this section, we demonstrate the proposed volume fraction procedure achieves the theoretical rate of convergence for two simple geometries, a unit sphere and a hemispherically capped oblique cylinder, inserted into two example background meshes, an axis-aligned hexahedral mesh and the same mesh with a sinusoidal perturbation applied to its coordinates. The axis-aligned mesh is defined by the domain  $\{\mathbf{x} : \mathbf{x} \in [-2, 2]^3\}$  with  $32^3$  cubical elements. The sinusoidally perturbed mesh applies the coordinate transformations

$$\begin{aligned} x &= x + 0.1 \sin(1/2\pi yz), \\ y &= y + 0.1 \sin(1/2\pi xz), \\ z &= z + 0.1 \sin(1/2\pi xy). \end{aligned} \tag{4}$$

to each vertex of the axis-aligned mesh. The unit sphere is centered at the origin. The hemispherically capped cylinder is defined as all points within a radius  $r = 0.2$  of the line segment defined by the two end points  $[-0.51, -0.49, -0.52]$  and  $[0.49, 0.51, 0.48]$ . For context, Figure 4 illustrates the two considered geometries, as represented by inserted volume fractions, in the sinusoidally perturbed mesh.

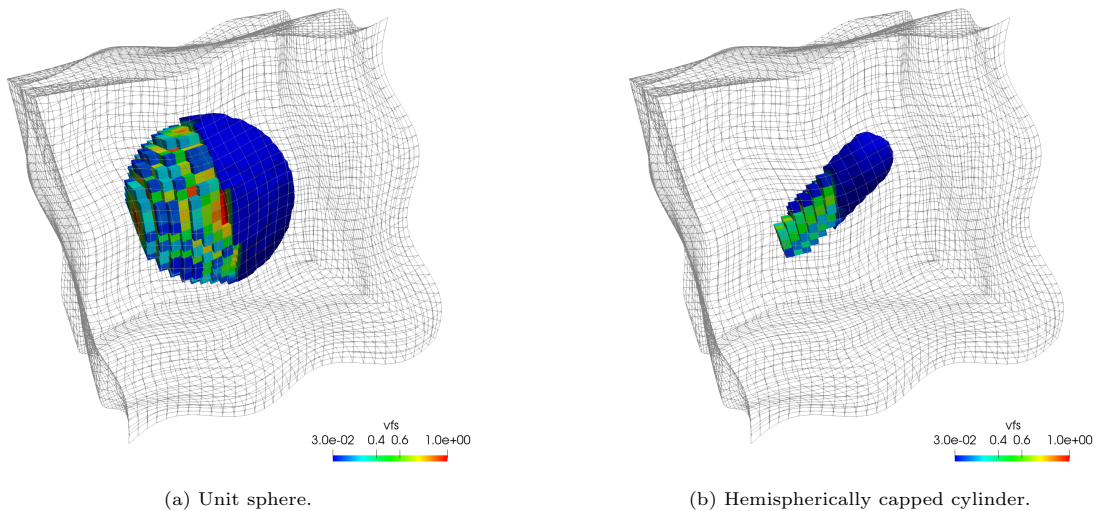


Figure 4: Representations of the verification geometries inserted into a sinusoidally perturbed mesh where the left portion of the domain is rendered with cell volume fractions and the right portion of the domain corresponds to a recovered isosurface.

The left-most plots of Figures 5 and 6 demonstrate the convergence behavior for each geometry inserted into each mesh using either the proposed spatially-accelerated AMR volume fraction insertion procedure or the simpler uniform sampling approach. For each approach, we measure the relative error,  $|V_h - V_{\text{exact}}|/V_{\text{exact}}$ , when using a maximum of  $n_{\text{sub}} = \{0, 1, 2, 3, 4, 5\}$  hex subdivisions, or correspondingly  $n_s = \{1, 8, 64, 512, 4096, 32768\}$  sampling points per element for the uniform sampling approach. In each of these four plots, we observe that the AMR plane sampling procedure achieves the theoretical second order convergence rate. Additionally, the relative error for both geometries inserted into the axis-aligned mesh is lower for the AMR plane sampling approach when compared to uniform sampling at all subdivision numbers. The left-most plots of Figure 5 demonstrates that the uniform sampling procedure does not always monotonically decrease the relative error when increasing the number of sampling points. This can be problematic when trying to achieve greater accuracy in a volume representation, as it may necessitate costly trial and error samplings with an unknown number of uniform subdivisions to achieve a desired error.

The bottom-left plot of Figure 5 shows that the uniform sampling approach is more accurate at 1 subdivision level than the AMR plane sampling approach and the bottom-left plot of Figure 6 shows that the uniform sampling approach is more accurate at nearly all measured subdivision levels. However, this perceived lack of performance of the AMR plane sampling approach can be explained when considering

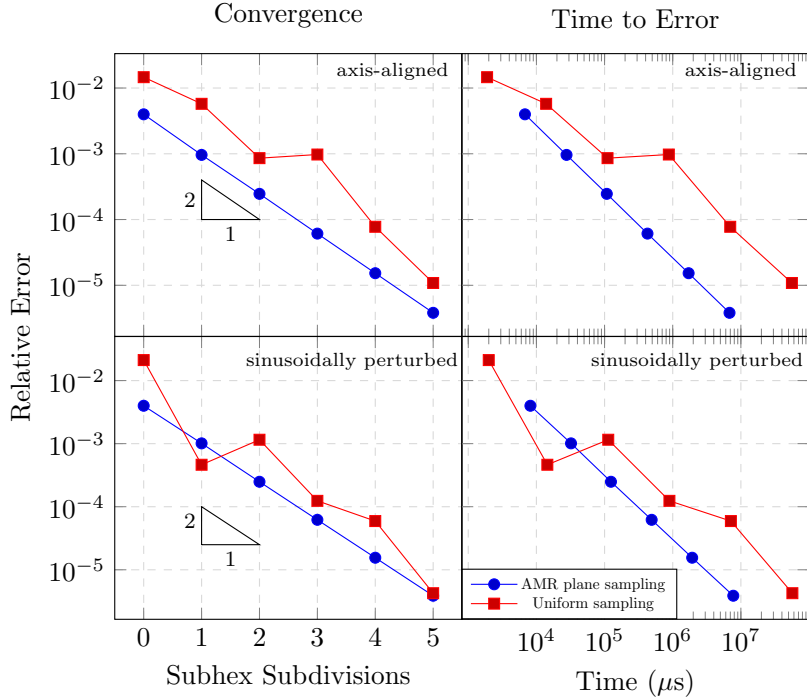


Figure 5: Convergence history (left) and time to solution (right) for a sphere inserted into an axis-aligned mesh (top) and a sinusoidally perturbed mesh (bottom) for the proposed volume fraction insertion procedure compared to a uniform sampling procedure.

computational complexity and time-to-error of each volume fraction sampling approach. The uniform sampling procedure scales as  $\mathcal{O}(n_{\text{sub}}^3)$  while the AMR plane sampling approach scales as  $\mathcal{O}(n_{\text{sub}}^2)$  since it refines locally to surface features.

The right-most plots of Figures 5 and 6 demonstrate the amount of computational time needed to achieve a given relative volume insertion error. In all scenarios, the right-most data point for the AMR plane sampling approach achieves a more accurate volume insertion in less amount of time when considering a constant error. This efficiency is most pronounced in upper-right plot of Figure 6 (corresponding to the hemispherically capped cylinder inserted into the axis-aligned mesh), where the time-to-error for the AMR plane sampling procedure is multiple orders of magnitude faster than uniform sampling. This efficacy is least pronounced in the bottom-right plot of Figure 6 (corresponding to the hemispherically capped cylinder inserted into the sinusoidally perturbed mesh), where the time-to-error for the AMR plane sampling procedure is slightly less than an order of magnitude faster than uniform sampling.

The  $x$ -axis distance between data points in the right-most plots of Figures 5 and 6 illustrates that each successive subdivision increases the time to solution by about a factor of about 8 for the uniform sampling approach, whereas this increase is only about a factor of 4 for the AMR plane sampling approach. This agrees with the computational complexity of the two approaches, as discussed previously. These plots illustrate that uniform sampling can be a valid and cost-effective approach if higher volumetric insertion errors are acceptable, but may become cost-prohibitive as errors are driven to lower and lower values.

#### 4.2. A Gear into an Unstructured Mesh

In this section, we investigate the accuracy and performance of the proposed volume fraction insertion procedure applied to a more complicated gear geometry, as shown by the left image in Figure 7. As a first



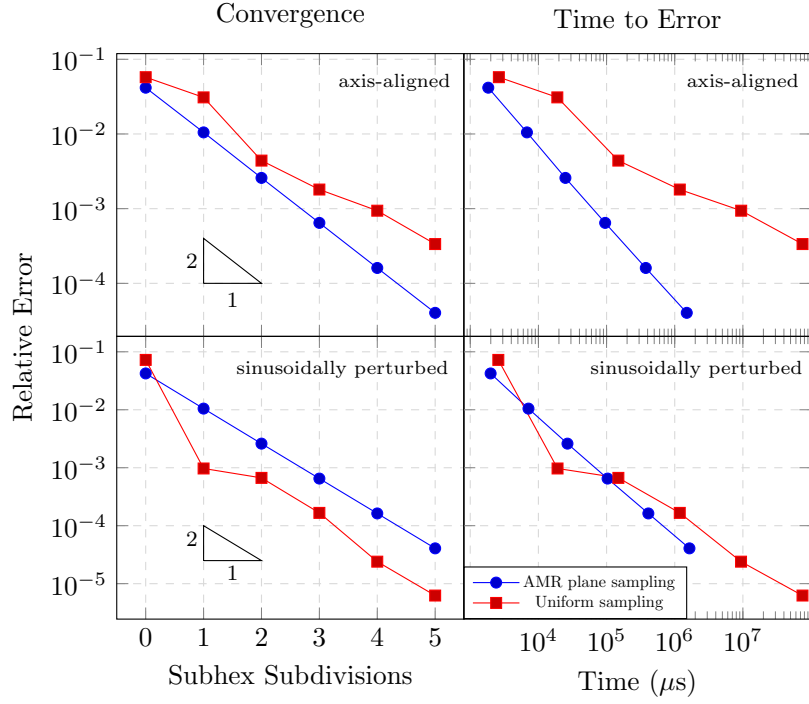
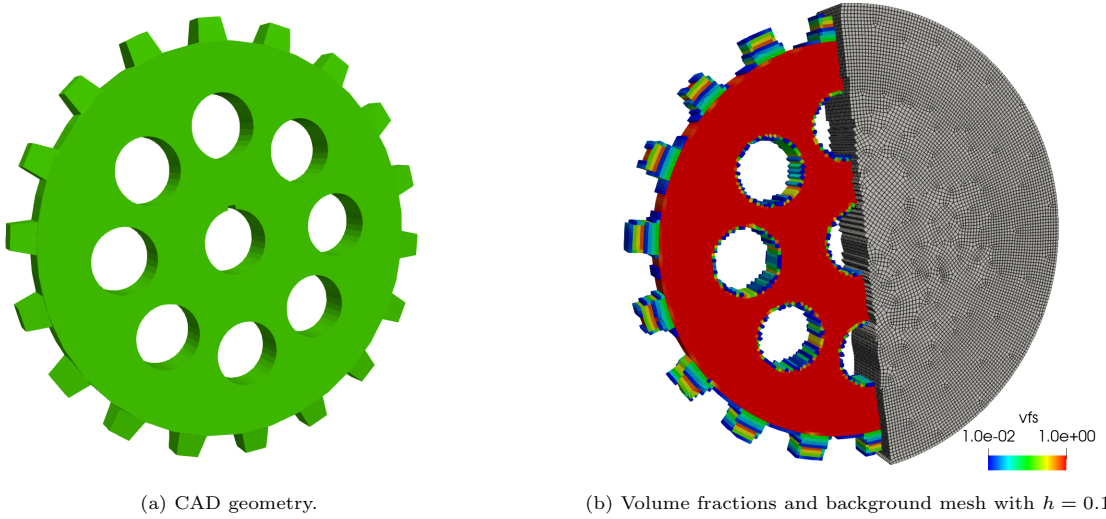


Figure 6: Convergence history (left) and time to solution (right) for a spherically capped cylinder inserted into an axis-aligned mesh (top) and a sinusoidally perturbed mesh (bottom) for the proposed volume fraction procedure compared to a uniform sampling procedure.



(a) CAD geometry.

(b) Volume fractions and background mesh with  $h = 0.1$ .

Figure 7: Illustrations of a gear geometry, a background unstructured hexahedral mesh, and the volume fractions obtained by the proposed insertion method using two AMR subdivisions.

test, the CAD geometry is inserted into several meshes of with characteristic element size  $h = \{0.2, 0.1, 0.05\}$ , where the background mesh for  $h = 0.1$  is shown in the right image in Figure 7. For this test, a fixed number of AMR subdivisions is chosen as  $n_{\text{sub}} = 2$ . Table 1 provides information about the AMR plane sampling

$h$	total hexes	hexes hit	subhexes hit	speedup
0.2	41380	11180	578288	4.57x
0.1	324440	60504	2424304	8.57x
0.05	2493320	234490	9359392	17.05x

Table 1: Statistics for gear CAD geometry inserted into different meshes.

	MAX	MIN	AVG
time (s)	129.367	13.780	72.485

Table 2: Timing statistics over MPI ranks for the volume insertion of the dynamic screw pinch geometry into a 12 million element mesh spread amongst 32 MPI ranks (as performed on a cluster with Intel Xeon Platinum 8260 2.40GHz processors).

procedure. The second column of Table 1 corresponds to the number of leaf nodes that are visited in the  $k$ -d tree during the sampling procedure, and illustrates that only a subset of the total hexahedra intersect the CAD geometry’s surface. The third column of Table 1 corresponds to the number of subhexahedra at the finest AMR subdivision level that intersect the CAD geometry’s surface and the final column corresponds to the theoretical speedup,  $(2^{n_{\text{sub}}})\text{total hexes}/\text{subhexes hit}$ , of the AMR sampling procedure when compared to naïvely performing the same plane sampling approach at every possible subhexahedron in the mesh.

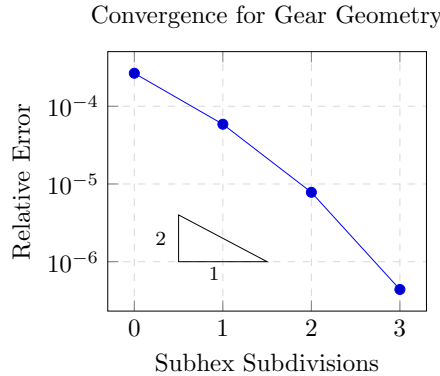


Figure 8: Convergence history for the gear geometry inserted into a background mesh of characteristic mesh size of  $h = 0.1$  using several maximum AMR subdivision levels.

As a second test, we again verify that the AMR plane sampling procedure achieves increased accuracy as the number of AMR subdivisions increases. In this test, the gear geometry is inserted into a single mesh with characteristic mesh size of  $h = 0.1$ , as shown by the right image of Figure 7 using the number of AMR subdivisions  $n_{\text{sub}} = \{0, 1, 2, 3\}$ . Figure 8 illustrates that the relative error  $\frac{|V_h - V_{\text{exact}}|}{V_{\text{exact}}}$  decreases at least quadratically as the number of AMR subdivisions increases. The reference CAD volume  $V_{\text{exact}}$  is reported by the CAD kernel as  $V_{\text{exact}} = 93.1818095$ . In terms of performance, the right-most data point in Figure 8 took a total of 262.3 seconds to complete. As a comparison, the uniform sampling approach with  $n_{\text{sub}} = 2$  uniform subdivisions, or  $n_s = 64$  sampling points per element, achieved a relative error of  $7.305 \times 10^{-4}$  in 564.8 seconds, more than twice the time required for the most accurate AMR sampling data point. Lastly, the construction of the  $k$ -d tree took 0.14 seconds, less than a tenth of a percent of the total volume fraction insertion runtime.

### 4.3. An Example with MPI Parallelism

In this section, we investigate inserting a complex geometry using a mesh with a distributed memory decomposition to demonstrate that the volume fraction insertion procedure is applicable on high-performance computing architectures. We consider a dynamic screw pinch geometry [13] inserted into an unstructured mesh of cylinder with 12.29 million elements partitioned over 32 MPI ranks using recursive inertial bisection [5, 14]. The left image of Figure 9 illustrates this geometry as represented by volume fractions, where colors refer to distinct mesh partitions. We use the proposed volume fraction insertion procedure with  $n_{\text{sub}} = 0$  adaptive subdivisions. The volume fraction sampling proceeds by loading each mesh part onto a corresponding single MPI rank, while the entire CAD geometry is loaded onto all MPI ranks. Individual  $k$ -d trees are then constructed for each mesh part independently (so that there is a forest of  $k$ -d trees) and the remainder of the volume fraction sampling proceeds as previously described.

Table 2 illustrates the maximum, minimum, and average runtime taken to perform the volume fraction insertion over the 32 MPI ranks. The ratio of the maximum runtime is close to an order of magnitude larger than the minimum runtime, which highlights an important point. The density of the geometry within the background mesh is, in general, completely independent of the background mesh itself, which could potentially lead to large load imbalances during the volume fraction insertion process. It may be possible to consider partitioning the CAD geometry itself in the same manner as the mesh, but we leave this as an avenue for future work. Additionally, if multiple CAD geometries are inserted in this partitioned context, such a load imbalance may eventually be unavoidable. The right image of Figure 9 illustrates a cutaway of an isovolume reconstructed from the inserted volume fractions. Lastly, for most physics applications, the geometry insertion process is a single-time upfront cost, which can also ameliorate the negative effects of load imbalance.

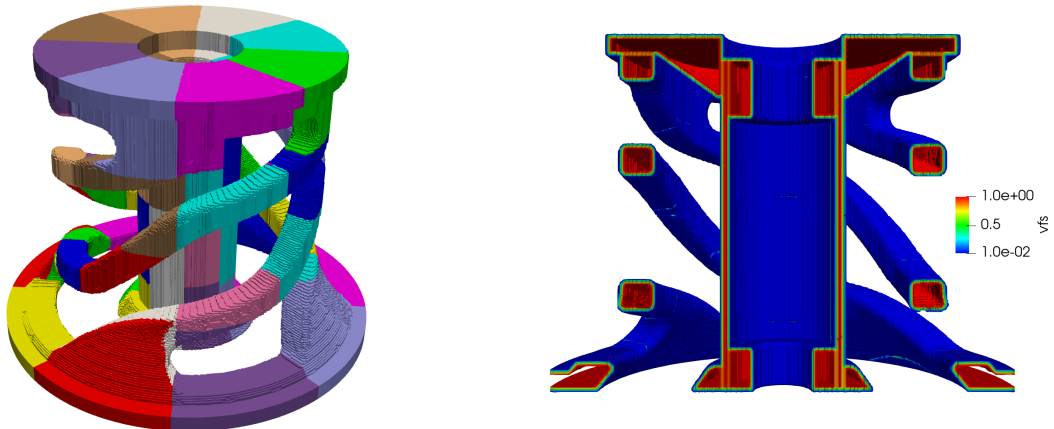


Figure 9: Left: the dynamic screw pinch geometry as inserted into an MPI-partitioned mesh with 32 parts where each color corresponds to an individual mesh part. Right: a cutaway of an isovolume reconstruction of the inserted dynamic screw pinch geometry into a large unstructured mesh.

## 5. Conclusions

In this paper, we have developed a spatially accelerated approach to represent three-dimensional CAD geometries by volume fractions in background hexahedral meshes. The approach proceeds in two steps. The first step involves assigning volume fractions for large subsets of hexahedra that are either entirely inside or outside of the CAD geometry through the use of a  $k$ -d tree. The second step involves assigning volume fractions to elements that intersect the CAD geometry’s surface by adaptively refining such elements. At the finest AMR subdivision level, the CAD surface is approximated linearly as a plane and subvolume fractions

are computed by intersecting a plane with a subhexahedra. An accurate volume fraction representation is then found by combining all subvolume fractions.

We have emphasized that this procedure requires only two queries from a CAD kernel. First, it is necessary to determine whether or not a spatial coordinate is inside or outside of the CAD geometry. Second, it is necessary to find the closest point on the CAD geometry's surface to a given input spatial coordinate. We then proved that the proposed procedure is second-order accurate for sufficiently smooth geometries and sufficiently refined background meshes.

To illustrate the procedure's effectiveness, we first considered two simple geometries, a sphere and a hemispherically capped cylinder, inserted into axis-aligned and non-axis aligned meshes. For all cases, the proposed volume fraction insertion procedure achieved the theoretical second-order convergence rate. Additionally, we've compared the proposed volume fraction insertion procedure to a simpler uniform in/out sampling procedure and demonstrated that, in most cases, the proposed procedure achieves greater accuracy in less computational runtime. We have additionally demonstrated the utility of the approach for two more realistic geometric examples.

Lastly, we remark that the current work need not be limited to hexahedral meshes. For instance, extensions to tetrahedral meshes would be trivial. In fact, provided a bounding sphere can be computed and a uniform refinement pattern exists for an individual element, the proposed procedure can be applied to arbitrary element types. As an avenue for future work, we propose applying the procedure to mixed element type meshes. Additionally, algorithms for more sophisticated moment-of-fluid volume representations could be developed and investigated. Finally, more sophisticated spatial acceleration data structures could be considered rather than the simple  $k$ -d tree we have considered presently.

## References

- [1] Michael J. Aftosmis, Marsha J. Berger, and John E. Melton. Robust and efficient Cartesian mesh generation for component-based geometry. *AIAA Journal*, 36(6):952–960, 1998.
- [2] Hyung Taek Ahn and Mikhail Shashkov. Adaptive moment-of-fluid method. *Journal of Computational Physics*, 228(8):2792–2821, 2009.
- [3] Jon Louis Bentley. Multidimensional binary search trees used for associative searching. *Communications of the ACM*, 18(9):509–517, 1975.
- [4] Thomas H. Cormen, Charles E. Leiserson, Ronald L. Rivest, and Clifford Stein. *Introduction to Algorithms*. MIT press, 2022.
- [5] Karen Devine, Erik Boman, Robert Heaphy, Bruce Hendrickson, and Courtenay Vaughan. Zoltan data management services for parallel dynamic applications. *Computing in Science and Engineering*, 4(2):90–97, 2002.
- [6] Vadim Dyadechko and Mikhail Shashkov. Reconstruction of multi-material interfaces from moment data. *Journal of Computational Physics*, 227(11):5361–5384, 2008.
- [7] Cyril W. Hirt and Billy D. Nichols. Volume of fluid (vof) method for the dynamics of free boundaries. *Journal of computational physics*, 39(1):201–225, 1981.
- [8] Alec Jacobson, Ladislav Kavan, and Olga Sorkine-Hornung. Robust inside-outside segmentation using generalized winding numbers. *ACM Transactions on Graphics (TOG)*, 32(4):1–12, 2013.
- [9] Matthew Jemison, Mark Sussman, and Mikhail Shashkov. Filament capturing with the multimaterial moment-of-fluid method. *Journal of Computational Physics*, 285:149–172, 2015.
- [10] John H.J. Niederhaus, Steven W. Bova, James B. Carleton, John H. Carpenter, Kyle R. Cochrane, Michael M. Crockett, Wen Dong, Timothy J. Fuller, Brian N. Granzow, Daniel A. Ibanez, Michael J. Powell, et al. Alegra: Finite element modeling for shock hydrodynamics and multiphysics. *International Journal of Impact Engineering*, page 104693, 2023.
- [11] Devon Powell and Tom Abel. An exact general remeshing scheme applied to physically conservative voxelization. *Journal of Computational Physics*, 297:340–356, 2015.
- [12] William J. Rider and Douglas B. Kothe. Reconstructing volume tracking. *Journal of Computational Physics*, 141(2):112–152, 1998.
- [13] Gabriel A. Shipley, Christopher A. Jennings, and Paul F. Schmit. Design of dynamic screw pinch experiments for magnetized liner inertial fusion. *Physics of Plasmas*, 26(10), 2019.
- [14] Horst D. Simon and Shang-Hua Teng. How good is recursive bisection? *SIAM Journal on Scientific Computing*, 18(5):1436–1445, 1997.
- [15] Jacob Spainhour, David Gunderman, and Kenneth Weiss. Robust containment queries over collections of rational parametric curves via generalized winding numbers. *ACM Transactions on Graphics (TOG)*, 43(4):1–14, 2024.
- [16] K. Weiss, G. Zagaris, R. Rieben, and A. Cook. Spatially accelerated shape embedding in multimaterial simulations. Technical report, Lawrence Livermore National Lab.(LLNL), Livermore, CA (United States), 2016.